INSTITUT DE FRANCE
Académie des sciences

Comptes Rendus

Chimie

Qichao Wu, Rongli Jiang, Huaiwen Liu, Xiaojiang Li and Dan Xie

Facile synthesis of core–shell porous Fe_3O_4@carbon microspheres with high lithium storage performance

Volume 23, issue 4-5 (2020), p. 279-289

Published online: 23 September 2020
Issue date: 10 November 2020

https://doi.org/10.5802/crchim.18

Les Comptes Rendus. Chimie *sont membres du*
Centre Mersenne pour l'édition scientifique ouverte
www.centre-mersenne.org
e-ISSN : 1878-1543

Comptes Rendus
Chimie
2020, 23, nº 4-5, p. 279-289
https://doi.org/10.5802/crchim.18

Full paper / *Mémoire*

Facile synthesis of core–shell porous Fe_3O_4@carbon microspheres with high lithium storage performance

Qichao Wu [a], Rongli Jiang*, [a], Huaiwen Liu [a], Xiaojiang Li [a] and Dan Xie [a]

[a] College of Chemical Engineering and Technology, China University of Mining and Technology, No. 1, Daxue Road, Xuzhou City 221116, Jiangsu Province, China

E-mails: wqcchemistry16@163.com (Q. Wu), ronglij@cumt.edu.cn (R. Jiang), liuhuaiwen.cn@gmail.com (H. Liu), lxjchemistry19@163.com (X. Li), xdchemistry19@163.com (D. Xie)

Abstract. Core–shell porous Fe_3O_4@C (CP-Fe_3O_4@C) microspheres were synthesized using an environmentally viable hydrothermal method. Carbonization can reduce Fe_2O_3 and provide a conductive coating simultaneously. CP-Fe_3O_4@C microspheres as an active material for Lithium-ion batteries demonstrate pseudocapacity for improved rate performance. With a distinct nanostructure and pseudocapacitive effect, the CP-Fe_3O_4@C microspheres show excellent electrochemical performance (~785 mAh·g^{-1} at 0.3 A·g^{-1} after 200 cycles). Capacity measurements of CP-Fe_3O_4@C microspheres suggest near 90% pseudocapacitance at relatively low scan rates (5 mV·s^{-1}).

Keywords. Lithium-ion batteries, Fe_3O_4, Porous core–shell structures, Carbon.

Manuscript received 18th December 2019, revised 12th February 2020, accepted 14th February 2020.

1. Introduction

Microelectronic technology continues to advance in the 21st century, with an increase in the number of microelectronic devices and a higher consumer demand for power sources. Lithium-ion batteries (LIBs) have clear and obvious advantages and continue to dominate the market [1–4]. Transition metal oxides were considered for LIB anode materials in early 2000 due to their high capacities stemming from conversion reaction mechanisms [5–7]. Fe_3O_4 was among these early studied anode materials with a high capacity (theoretical value 926 mAh·g^{-1}) [8–10]. However, during cycling, Fe_3O_4 expands and breaks, causing rapid loss of capacity. Additionally, the conductivity of Fe_3O_4 is poor [11]. Carbon coating was found to help alleviate these problems, both addressing Fe_3O_4 volume expansion during cycling and preventing particle agglomeration [12–14]. More importantly, the carbon layer not only improved the conductivity of the electrode but also stabilized the solid electrolyte interface (SEI), which greatly improved the cycle life and rate capability of LIBs [15–17]. Further research in materials design pushed for Fe_3O_4 with a porous or hollow structure, which improves electrode reversibility and active material/electrolyte contact [18–20]. Recently, Wang *et al.* reported a novel Fe_3O_4@Carbon yolk–shell nanorod anode material by a one-pot method. The voids in the Fe_3O_4@Carbon core–shell nanorods were beneficial for volume expansion and allowed the Fe_3O_4@Carbon-based electrode to maintain its structural integrity during repeated Li^+ in-

* Corresponding author.

sertion/extraction. Additionally, carbon coating on Fe_3O_4 provided a stable SEI film. The Fe_3O_4@Carbon composites exhibited high mechanical stability and excellent cycling performance (954 mAh·g^{-1} 200 cycles at 0.5 A·g^{-1}) [21]. Liu *et al.* prepared micron-sized porous Fe_3O_4 spheres through the solvothermal and calcination methods. Carbon-covered Fe_3O_4 porous microspheres demonstrated an outstanding reversible capacity (747 mAh·g^{-1} after 50 cycles at 0.1 A·g^{-1}) and good rate capacity (255 mAh·g^{-1} at 1.6 A·g^{-1}) [22]. Zhou *et al.* synthesized uniform porous Fe_3O_4@Carbon microspheres by a hydrothermal method. These microspheres showed good electrochemical performance (609 mAh·g^{-1} after 200 cycles at 0.2 A·g^{-1}) [23].

In this work, novel core–shell porous Fe_3O_4@C microspheres (CP-Fe_3O_4@C) were successfully designed and constructed by simple hydrothermal and carbonization methods. First, the Fe_3O_4@GU microspheres were synthesized using ferric chloride as an iron source and common chemicals glucose and urea as filler particles; the Fe_3O_4@GU composite was heat-treated in oxygen atmosphere to obtain the porous Fe_2O_3 microspheres. Second, resorcinol-formaldehyde (RF) resin was applied to porous Fe_2O_3 microspheres to obtain core–shell Fe_2O_3@RF microspheres, which were then used for the fabrication of CP-Fe_3O_4@C microspheres by one-step carbonization without a surfactant. The material synthesized through our straightforward method shows excellent performance as an anode material for LIBs.

2. Experimental section

2.1. *Preparation of Fe_3O_4@GU*

The Fe_3O_4@GU microspheres were prepared by a simple hydrothermal technique. Briefly, 2.13 g of ferric chloride ($FeCl_3$), 2.0 g of glucose ($C_6H_{12}O_6$) and 2.1 g of urea (CH_4N_2O) were added to 90 mL of deionized (DI) water and stirred. The resulting orange solution was placed into a 200 mL stainless steel Teflon-lined autoclave, heated at 200 °C for 6 h and then cooled to ambient temperature. The black Fe_3O_4@GU microspheres were washed with DI water thrice and dried at 60 °C for 12 h.

2.2. *Preparation of porous Fe_2O_3*

The Fe_3O_4@GU microspheres were heated at 500 °C in oxygen for 4 h, after which the furnace was cooled to the ambient temperature naturally. The bright orange porous Fe_2O_3 microspheres were washed with DI water thrice and dried at 60 °C for 12 h.

2.3. *Preparation of CP-Fe_3O_4@C microspheres*

A mixture containing 15 mL of DI water and 15 mL of ethanol was used to disperse porous Fe_2O_3 microspheres. Then, 2 mL of formaldehyde and 0.8 g of resorcinol were added, and the whole mixture was stirred for 30 min. The mixture was then transferred into a 100 mL stainless steel Teflon-lined autoclave and heated at 100 °C for 36 h. The resulting material (which was Fe_2O_3@RF composite) was calcined at 500 °C for 4 h under N_2 at a heating rate of 2 °C·min^{-1} to produce CP-Fe_3O_4@C microspheres. A schematic of the the preparation process for CP-Fe_3O_4@C microspheres is shown in Figure 1.

2.4. *Material characterization*

Crystalline phases were confirmed by X-ray diffraction (XRD) using Cu K_α radiation (λ = 0.15406 nm) by a D8 type advanced diffractometer (40 kV and 30 mA). X-ray photoelectron spectroscopy (XPS) was performed at 280 eV using ESCALAB 250Xi operated using Al K_α radiation as an excitation source. Morphology and microstructure were characterized by field emission scanning electron microscopy (FE-SEM, Merlin Compact) and transmission electron microscopy (TEM, G2F20). Raman spectra were recorded using the Bruker-Senterra spectrometer with 514 nm laser excitation. Sample weight losses were measured by thermo-gravimetric analysis (TGA, HCT-3). The analysis was performed in air in a range of 30 to 800 °C at a heating rate of 10 °C·min^{-1}. The surface area of the CP-Fe_3O_4@C composite was measured by the Brunauer–Emmett–Teller (BET) method (Autosorb-IQ). Pore sizes were obtained from the corresponding nitrogen adsorption/desorption isotherms using the Barrett–Joyner–Halenda formula.

2.5. *Electrochemical measurements*

Anodes were prepared by mixing the active materials with conductive acetylene black and poly-vinylidene

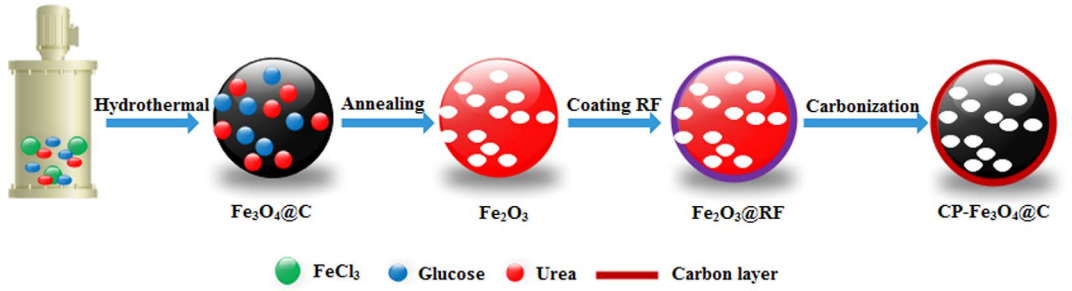

Figure 1. Synthesis flow chart of the CP-Fe_3O_4@C composite.

fluoride (PVDF) binder at a ratio of 8:1:1. The N-methyl pyrrolidone solvent (1.0 mL) was added to prepare slurry, which was applied to a copper foil and dried at 80 °C for 12 h. Coin cells (with standard size 2032) were assembled in a glove box under Ar atmosphere. Metallic Li was used as the counter electrode. The $LiPF_6$ (1.0 M) dissolved in a 1:1 ethylene carbonate:dimethyl carbonate mixture was used as the electrolyte. Galvanostatic charge–discharge (GCD) measurements at various current densities were recorded using NEWARE CT-4008 (Shenzhen). Cyclic voltammetry (CV) was measured using an electrochemical workstation (Solartron 1287) from a potential of 0.01 to 3.00 V at a 0.1 $mV{\cdot}s^{-1}$ sweep rate. Electrochemical impedance spectroscopy was conducted on the electrochemical workstation (Solartron 1287) from 0.01 Hz to 100 kHz at a perturbation of 5 mV AC.

3. Results and discussion

As-prepared Fe_3O_4@GU, Fe_2O_3 and CP-Fe_3O_4@C microspheres were characterized by XRD (Figure 2a). The strong reflections of Fe_2O_3 microspheres observed at 2Θ = 24.2, 33.2, 35.7, 40.9, 49.5, 54.0, 62.4 and 64.0° correspond to the (012), (104), (110), (113), (024), (116), (214) and (330) planes of hematite (JCPDS 33-0664) [24]. The XRD of Fe_3O_4@GU and CP-Fe_3O_4@C microspheres showed several peaks that are consistent with the face-centered Fe_3O_4 phase (JCPDS 19-0624) [12,25]. In addition, no peaks of Fe_2O_3 were found in the diffraction peak of CP-Fe_3O_4@C, indicating that Fe_2O_3 was converted to Fe_3O_4. The carbon content analyses for Fe_3O_4@GU, Fe_2O_3 and CP-Fe_3O_4@C materials are shown in Figure 2b. Fe_2O_3 demonstrated almost no carbon weight loss and was corroborated by the XRD showing that only a Fe_2O_3 phase was present in this sample. There was rapid weight loss for Fe_3O_4@GU and CP-Fe_3O_4@C occurring from 200 to 400 °C, which was attributed to the decomposition of the carbon layer. With this weight loss, it was determined that the carbon content values for the Fe_3O_4@GU and CP-Fe_3O_4@C microspheres were 37.61% and 17.35%, respectively.

Raman spectra showed the presence of carbon in the CP-Fe_3O_4@C microspheres (see Supplementary Figure S1), indicated by the presence of two broad peaks at 1349 and 1587 cm^{-1}, which correspond to D and G bands. These bands are assigned to sp^3 disordered and sp^2 ordered graphitic carbon bonds [26]. The ratio between D and G bands (I_D/I_G) is often used to evaluate the degree of carbon graphitization. For the CP-Fe_3O_4@C microspheres, the ratio was 0.96, and this suggests a high degree of graphitization in the carbon coating of the Fe_3O_4 microspheres. This graphitization is beneficial for electrical conductivity of the composite [27].

The nitrogen absorption/desorption isotherms of CP-Fe_3O_4@C show a hysteresis from 0.5 to 1.0 relative pressure (see Figure 2c). The BET surface area of the CP-Fe_3O_4@C was equal to 16.8 $m^2{\cdot}g^{-1}$. The pore size distribution curve shows a peak near 3.8 nm (see insert in Figure 2c), evincing a nanopore presence. High surface area and porosity provide good contact between the electrode material and the electrolyte. This in turn promotes Li^+ diffusion and allows active material to adapt to the volume expansion [28].

The XPS of CP-Fe_3O_4@C microspheres shows peaks corresponding to Fe, C and O (see Figure 2d). High-resolution scans and curve fitting show Fe peaks at 711.2 and 724.8 eV, which belong to Fe $2p_{3/2}$

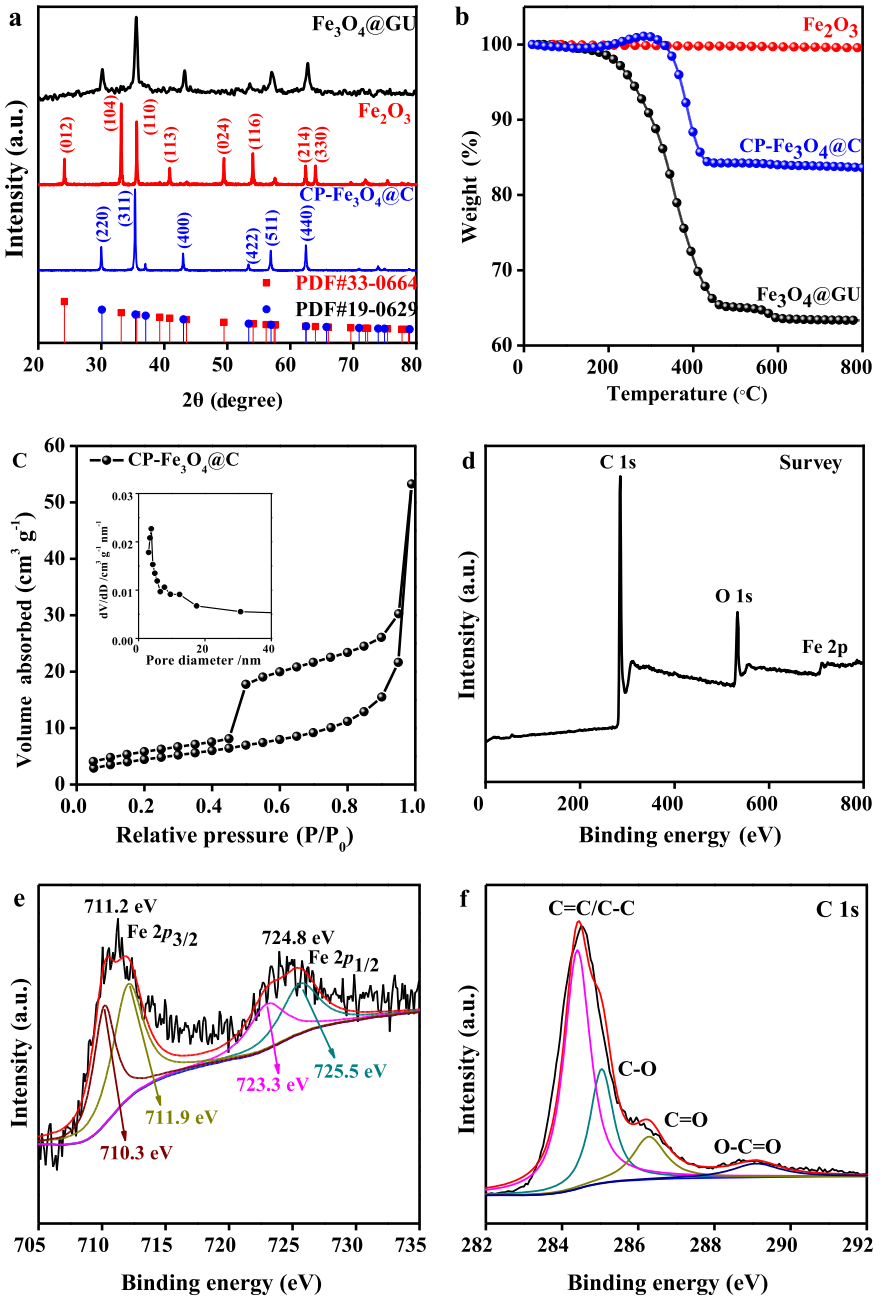

Figure 2. Sample characterization. (a) XRD pattern, (b) TGA pattern, (c) nitrogen adsorption/desorption isotherms and pore size distribution curve (inset), XPS spectra of the CP-Fe_3O_4@C (d) survey, (e) Fe 2p, (f) C 1s.

and Fe $2p_{1/2}$, respectively (see Figure 2e), which are typical of Fe_3O_4-based materials [29,30]. Two pairs of peaks at 710.3 and 723.3 eV and at 711.9 and 725.5 eV correspond to Fe $2p_{3/2}$ and Fe $2p_{1/2}$ of Fe^{2+} and Fe^{3+}, respectively [31]. High-resolution scans of C 1s (see Figure 2f) show peaks at 284.4 (typical of sp^2-hybridized graphitic C), 285.0 eV (attributed to the sp^3-hybridized C) and at 286.3 and

289.0 eV (both of which are attributed to the carbon layer surface functional groups such as C=O and O=C=O) [32].

The SEM of Fe_3O_4@GU microspheres demonstrated particles with uniform spherical shapes with an average diameter of 250 nm (see Figure 3a). After annealing, Fe_3O_4@GU microspheres were completely converted to Fe_2O_3 microspheres (Figure 3b) as supported by XRD. The surface of the Fe_2O_3 microspheres shows strong porosity unlike Fe_3O_4@GU microspheres. Micrographs of the CP-Fe_3O_4@C microspheres obtained after carbon coating of Fe_2O_3 microspheres are shown in Figure 3c. It can be seen that the surfaces of the CP-Fe_3O_4@C microspheres are smooth compared to those of the Fe_2O_3 microspheres because the carbon layer was successfully coated. Figures 3d, e and f are TEM images of Fe_3O_4@GU, Fe_2O_3 and CP-Fe_3O_4@C microspheres, respectively. From these three figures, it can be seen that both Fe_2O_3 and CP-Fe_3O_4@C microspheres show clear porosity, while Fe_3O_4@GU microspheres exhibit almost none. The TEM image of the CP-Fe_3O_4@C microspheres shows a thin carbon outer layer approximately 20 nm thick (see Supplementary Figure S2). High-resolution TEM images of the CP-Fe_3O_4@C microspheres (Supplementary Figure S3) show distinct lattice fringes with a spacing of 0.252 nm, which corresponds to the (311) planes of cubic Fe_3O_4. The scanning TEM image of the CP-Fe_3O_4@C microspheres (Figure 3g) and the corresponding element mapping (Figure 3h–j) further establish that CP-Fe_3O_4@C microspheres were successfully carbon-coated.

Cyclic voltammetry of the CP-Fe_3O_4@C electrode displays a definite reduction peak at 0.2–0.8 V during the first discharge (Figure 4a), which corresponds to the structural transformation caused by lithium incorporation according to the chemical reaction:

$$Fe_3O_4 + xLi^+ + xe^- \rightarrow Li_xFe_3O_4$$

Further conversion of $Li_xFe_3O_4$ to Fe(0) occurs according to the reaction [5,33]:

$$Li_xFe_3O_4 + (8-x)Li^+ + (8-x)e^- \rightarrow 4Li_2O + 3Fe$$

During subsequent cycles, lithium insertion at the cathode occurred mainly between 0.58 and 1.15 V, and lithium extraction at the anode mainly occurred between 1.38 and 2.11 V. It is worth noting that the 2nd, 3rd, and 10th cycles of CV almost coincide, indicating that the electrode cycling process has a minimal impact on subsequent cycles. Figure 4b shows the GCD of the CP-Fe_3O_4@C electrode after the 1st, 2nd, 3rd, 50th, 100th and 200th cycles at 0.3 $A{\cdot}g^{-1}$ between 0.01 and 3.0 V. The initial discharge curve showed a plateau between 0.21 and 0.66 V. The second and subsequent discharge voltages increased to 0.62–1.10 V, which is consistent with CV. The initial discharge and charge capacity of the CP-Fe_3O_4@C electrode were 1291 and 914 $mAh{\cdot}g^{-1}$. These drastic differences in capacity usually stem from the formation of the SEI and often occur during the first cycle. The stability and capacity of the CP-Fe_3O_4@C electrode were compared to those of the Fe_3O_4@GU and Fe_2O_3 electrodes (see Figure 4c). After 200 cycles at 0.3 $A{\cdot}g^{-1}$, the reversible capacities of the CP-Fe_3O_4@C, Fe_3O_4@GU and Fe_2O_3 electrodes were 785, 508 and 203 $mAh{\cdot}g^{-1}$, respectively. It is clear that the porous core–shell structure of the CP-Fe_3O_4@C electrode plays a critical role in the electrochemical performance. Experimentally obtained electrochemical characteristics of different Fe_3O_4@carbon electrodes with respect to their corresponding Li storage capacity are shown in Supplementary Table S1. The rate capability of the CP-Fe_3O_4@C electrode is shown in Figure 4d. The stable discharge capacities of the CP-Fe_3O_4@C electrode at 0.3, 0.8, 1.6, 3 and 6 $A{\cdot}g^{-1}$ were ~791, 648, 471, 312, and 130 $mAh{\cdot}g^{-1}$, respectively. Additionally, the discharge capacity value returned to 723 $mAh{\cdot}g^{-1}$ after the current density was reduced back to 0.3 $A{\cdot}g^{-1}$. These results demonstrate that the CP-Fe_3O_4@C electrode has outstanding rate capability, high reversibility, and stability for LIBs. Figure 4e shows the charge–discharge curves of the anodes containing CP-Fe_3O_4@C microspheres as the active material at various current densities. The charge–discharge voltage plateau gradually sloped as the current density was increased, but even at a current density of 6 $A{\cdot}g^{-1}$, the charge–discharge voltage plateaus still persisted.

The electrochemical impedance behavior of the CP-Fe_3O_4@C electrode under different current cycles at the same current density was studied using Nyquist plots (see Figure 4f). All plots exhibit semicircles in the high- and intermediate-frequency regions and oblique curves at low frequencies. Additionally, equivalent circuit modeling (top right insets,

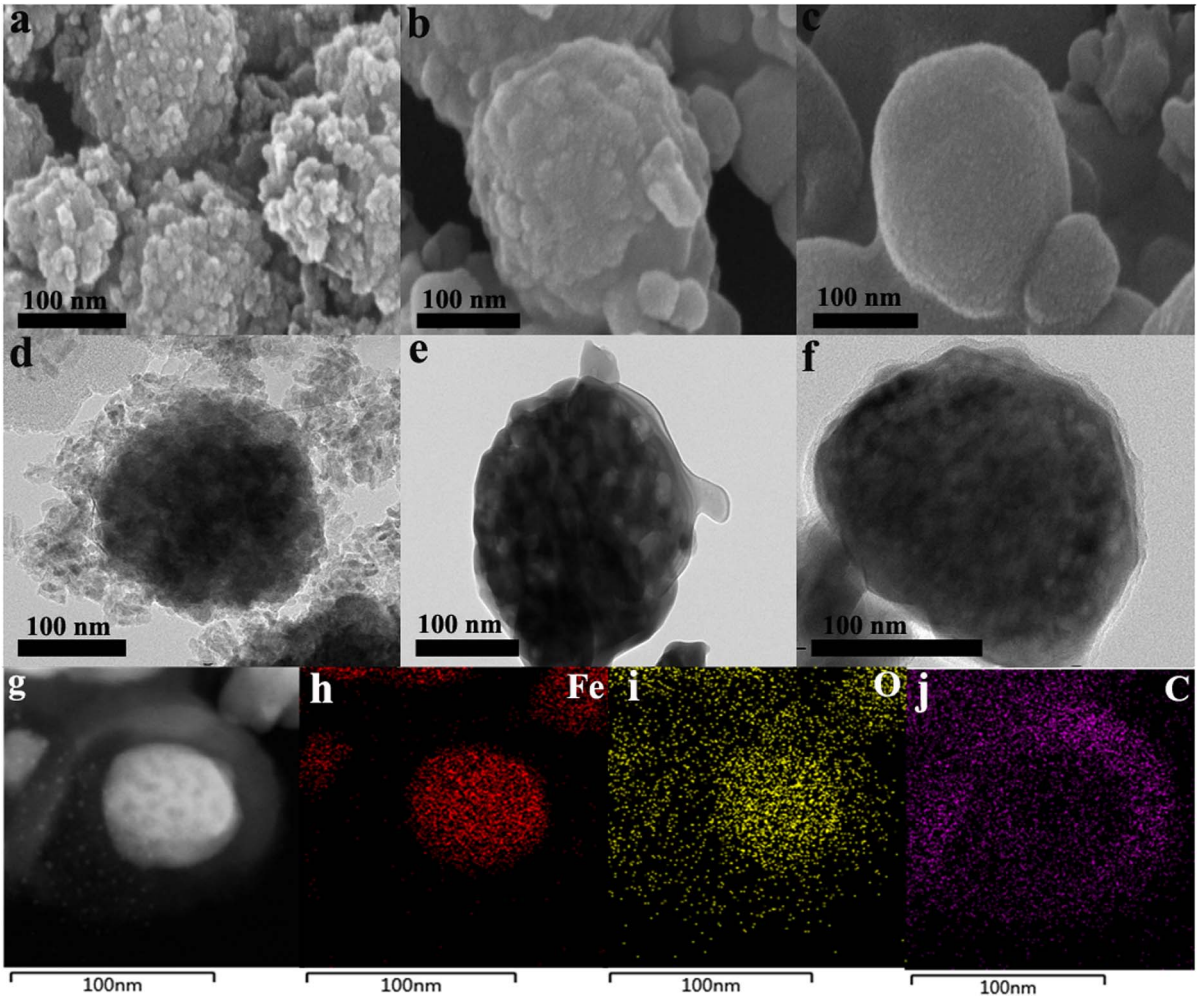

Figure 3. SEM images of (a) Fe_3O_4@GU, (b) Fe_2O_3 and (c) CP-Fe_3O_4@C composites. TEM images of (d) Fe_3O_4@GU, (e) Fe_2O_3 and (f) CP-Fe_3O_4@C composites. EDX elemental mapping of (g–j) CP-Fe_3O_4@C composite.

Figure 4f) was carried out using Z-VIEW software to obtain kinetic parameters of three composites. According to the equivalent circuit diagram, the intercept of the high-frequency semicircle with the x-axis corresponds to the electrolyte resistance (R_e), while R_f and R_{ct} correspond to SEI film and charge transfer resistances, respectively [27,34]. The slope at low frequencies corresponds to the Warburg impedance (Z_w) of the Li^+ diffusion; CPE1 and CPE2 are the SEI film and double layer capacitances, respectively [35, 36]. CP-Fe_3O_4@C-based anodes exhibited lower R_{ct} values (which were equal to 16.5 Ω) after the first cycle, especially when compared to R_{ct} values of the fresh cycle (which was equal to 395.7 Ω). This difference is mainly due to the wetting of the electrode and proper SEI formation during the first cycle. The R_{ct} value after the 200th cycle differs only slightly from the R_{ct} value after the 100th cycle, again pointing to an excellent electrode structural stability. Resistance values of electrodes based on Fe_3O_4@GU and Fe_2O_3 active materials were higher than the total resistance of the CP-Fe_3O_4@C-based electrodes for all cycles tested in this work (see Supplementary Figures S4a and S4b).

The rate performance of CP-Fe_3O_4@C-based LIB anodes as well as their reaction kinetics was analyzed

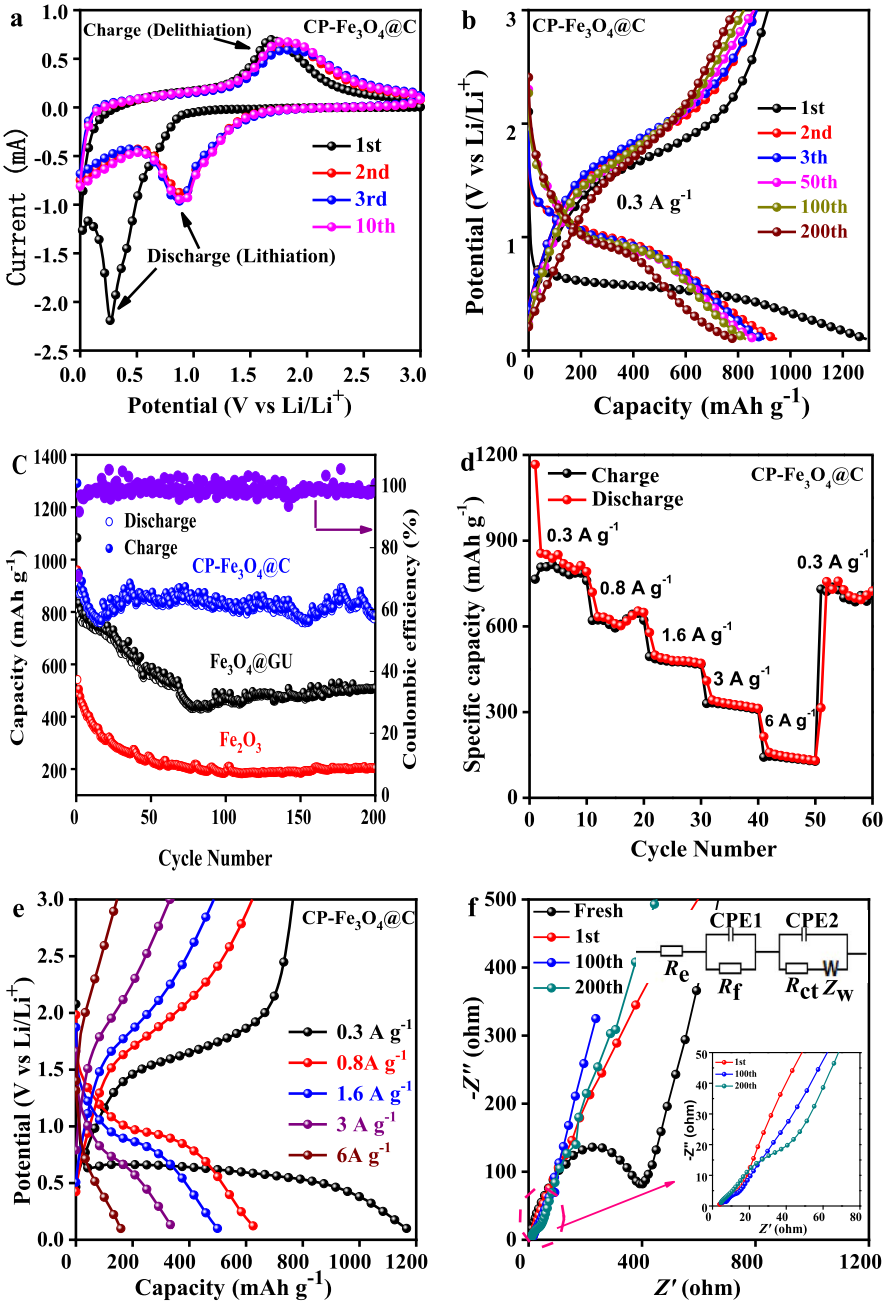

Figure 4. (a) CV curves at 0.1 mV·s^{-1} and (b) GCD curves at 0.3 A·g^{-1} of the CP-Fe_3O_4@C electrode. (c) Cyclic performance at 0.3 A·g^{-1} of the Fe_2O_3, Fe_3O_4@GU and CP-Fe_3O_4@C electrodes. (d) Rate performance at different current densities. (e) Representative discharge–charge voltage profiles at various rates. (f) Nyquist plots of the CP-Fe_3O_4@C electrode (top right insets show the equivalent circuit model).

by CV. The contribution of capacitance is calculated and identified using gradually increasing sweep rates during CV as shown in Figure 5a. Using the method of Dunn [37,38], the total current response (i) at con-

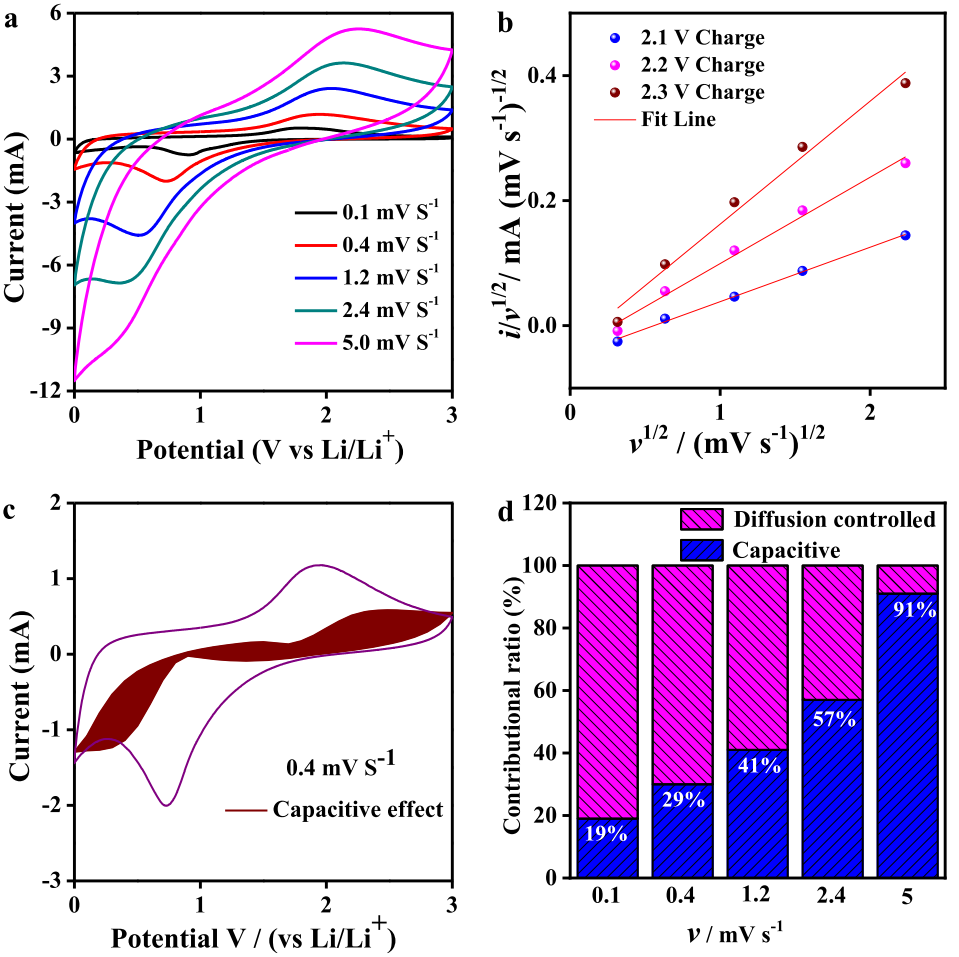

Figure 5. (a) CV curves at different scan rates from 0.1 to 5 mV·s^{-1}. (b) The fitted lines of $i(V)/v^{1/2}$ versus $i/v^{1/2}$ at different voltages. (c) CV curves with capacitive contribution at 0.4 mV·s^{-1}. (d) Separation of contributions from capacitive effects and diffusion-controlled capacities at different scan rates.

stant potential (V) can be represented as a combination of surface capacitive effects and diffusion-controlled insertion processes (see (1) and (2)):

$$i(V) = K_1 v + K_2 v^{1/2}, \quad (1)$$

$$i(V)/v^{1/2} = K_1 v^{1/2} + K_2, \quad (2)$$

where $K_1 v$ and $K_2 v^{1/2}$ are the contributions of the total surface capacitive and diffusion-controlled insertion processes, respectively. Comparing CV results at different sweeps, the values of K_1 and K_2 can be determined by fitting $i(V)/v^{1/2}$ versus $v^{1/2}$ as a linear function according to (2) as shown in Figure 5b. Subsequently, K_1 and K_2 are replaced by their values in (1), partitioning the contribution of Faradic capacity from the contribution of pseudocapacitance in the total stored charge. Figure 5c shows a separation of capacitance and diffusion currents at a scan rate of 0.4 mV·s^{-1}. Brown areas represent capacitance effect, and blank areas represent diffusion-controlled capabilities. As can be seen from Figure 5d, at 0.1, 0.4, 1.2, 2.4 and 5 mV·s^{-1}, pseudocapacitance accounts for 19%, 29%, 41%, 57% and 91%, respectively, of the total capacity, indicating significant pseudocapacitance behavior during the cycling of CP-Fe_3O_4@C-based anodes at high rates. Thus, CP-Fe_3O_4@C-based electrodes demonstrated higher pseudocapacitance contribution at almost all current densities, which is indicative of an excellent rate performance.

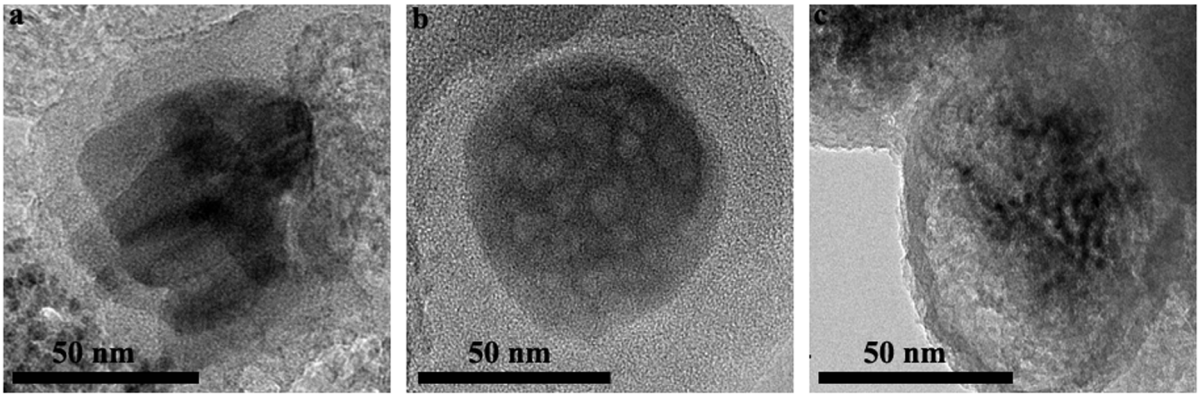

Figure 6. CP-Fe_3O_4@C electrode: (a) before cycle, (b) after 10 cycles and (c) after 60 cycles.

The morphology of the CP-Fe_3O_4@C-based electrode was tested before cycling and also after 10 and 60 cycles (Figure 6). Fe_3O_4 microspheres in prepared CP-Fe_3O_4@C electrode material are uniformly wrapped by a carbon layer (see Figure 6a). The carbon coating on the CP-Fe_3O_4@C electrode after the 10th cycle is still intact, and the carbon layer is mostly unchanged (see Figure 6b). After the 60th cycle, Fe_3O_4 structurally deteriorates into smaller microspheres, but Fe_3O_4 remains well coated with carbon layers (see Figure 6c).

4. Conclusions

In summary, the core–shell CP-Fe_3O_4@C microspheres were synthesized by simple methods using common inexpensive and easily removable chemicals as filler particles. The unique structural characteristics of the CP-Fe_3O_4@C microspheres yielded electrodes with capacities equal to 785 $mAh{\cdot}g^{-1}$ (at 0.3 $A{\cdot}g^{-1}$ after 200 cycles). In addition, it was further shown that the CP-Fe_3O_4@C electrode has excellent rate performance through reaction kinetics. These experimental results show that the CP-Fe_3O_4@C composite prepared by this simple method has strong prospects as an active anode material for high-performance LIBs.

Conflicts of interest

The authors declare no conflict of interest.

Acknowledgment

This research was supported by the Future Scientists Program of "Double First Class" of China University of Mining and Technology (No. 2019WLKXJ025).

Supplementary data

Supporting information for this article is available on the journal's website under https://doi.org/10.5802/crchim.18 or from the author.

References

[1] M. Armand, J. M. Tarascon, "Building better batteries", *Nature*, 2008, **451**, 652-657.

[2] M. Reddy, G. Rao, B. Chowdari, "Metal oxides and oxysalts as anode materials for Li ion batteries", *Chem. Rev.*, 2013, **113**, 5364-5457.

[3] Y. Fu, Y. He, L. Qu, Y. Feng, J. Li, J. Liu, G. Zhang, W. Xie, "Enhancement in leaching process of lithium and cobalt from spent lithium-ion batteries using benzenesulfonic acid system", *Waste Manage.*, 2019, **88**, 191-199.

[4] P. Poizot, S. Laruelle, S. Grugeon, L. Dupont, J. Tarascon, "Nano-sized transition-metal oxides as negative-electrode materials for lithium-ion batteries", *Nature*, 2000, **407**, 496-499.

[5] Y. Huang, Z. Xu, J. Mai, T.-K. Lau, X. Lu, Y.-J. Hsu, Y. Chen, A. C. Lee, Y. Hou, Y. S. Meng, Q. Li, "Revisiting the origin of cycling enhanced capacity of Fe_3O_4 based nanostructured electrode for lithium ion batteries", *Nano Energy*, 2017, **41**, 426-433.

[6] Q. Wu, R. Jiang, L. Mu, S. Xu, "Fe_3O_4 anodes for lithium batteries: production techniques and general applications", *C. R. Chim.*, 2019, **22**, 96-102.

[7] P. L. Taberna, S. Mitra, P. Poizot, P. Simon, J. M. Tarascon, "High rate capabilities Fe_3O_4-based Cu nano-architectured electrodes for lithium-ion battery applications", *Nat. Mater.*, 2006, **5**, 567-573.

[8] S. Yuan, X. Bo, L. Guo, "In-situ insertion of multi-walled carbon nanotubes in the Fe_3O_4/N/C composite derived from iron-based metal-organic frameworks as a catalyst for effective sensing acetaminophen and metronidazole", *Talanta*, 2019, **193**, 100-109.

[9] H. L. Karlsson, P. Cronholm, J. Gustafsson, L. Möller, "Copper oxide nanoparticles are highly toxic: a comparison between metal oxide nanoparticles and carbon nanotubes", *Chem. Res. Toxicol.*, 2008, **21**, 1726-1732.

[10] E. Kang, Y. S. Jung, A. S. Cavanagh, G.-H. Kim, S. M. George, A. C. Dillon, J. K. Kim, J. Lee, "Fe_3O_4 nanoparticles confined in mesocellular carbon foam for high performance anode materials for lithium-ion batteries", *Adv. Funct. Mater.*, 2011, **21**, 2430-2438.

[11] T. Yoon, C. Chae, Y.-K. Sun, X. Zhao, H. H. Kung, J. K. Lee, "Bottom-up in situ formation of Fe_3O_4 nanocrystals in a porous carbon foam for lithium-ion battery anodes", *J. Mater. Chem.*, 2011, **21**, 17325-17330.

[12] G. Zhou, D.-W. Wang, F. Li, L. Zhang, N. Li, Z. S. Wu, L. Wen, G. Q. Lu, H.-M. Cheng, "Graphene-wrapped Fe_3O_4 anode material with improved reversible capacity and cyclic stability for lithium ion batteries", *Chem. Mater.*, 2010, **22**, 5306-5313.

[13] J. Su, M. Cao, L. Ren, C. Hu, "Fe_3O_4-graphene nanocomposites with improved lithium storage and magnetism properties", *J. Phys. Chem. C*, 2011, **115**, 14469-14477.

[14] E. Yoo, J. Kim, E. Hosono, H.-S. Zhou, T. Kudo, I. Honma, "Large reversible Li storage of graphene nanosheet families for use in rechargeable lithium ion batteries", *Nano Lett.*, 2008, **8**, 2277-2282.

[15] D. Golberg, Y. Bando, Y. Huang, T. Terao, M. Mitome, C. Tang, C. Zhi, "Boron nitride nanotubes and nanosheets", *ACS Nano*, 2010, **4**, 2979-2993.

[16] J. Luo, J. Liu, Z. Zeng, C. F. Ng, L. Ma, H. Zhang, J. Lin, Z. Shen, H. J. Fan, "Three-dimensional graphene foam supported Fe_3O_4 lithium battery anodes with long cycle life and high rate capability", *Nano Lett.*, 2013, **13**, 6136-6143.

[17] X. Lu, R. Wang, Y. Bai, J. Chen, J. Sun, "Facile preparation of a three-dimensional Fe_3O_4/macroporous graphene composite for high-performance Li storage", *J. Mater. Chem. A*, 2015, **3**, 12031-12037.

[18] P. Salimi, O. Norouzi, S. E. M. Pourhosseini, "Two-step synthesis of nanohusk Fe_3O_4 embedded in 3D network pyrolytic marine biochar for a new generation of anode materials for lithium-ion batteries", *J. Alloys Compd.*, 2019, **786**, 930-937.

[19] S. E. M. Pourhosseini, O. Norouzi, P. Salimi, H. R. Naderi, "Synthesis of a novel interconnected 3D pore network algal biochar constituting iron nanoparticles derived from a harmful marine biomass as high-performance asymmetric supercapacitor electrodes", *ACS Sustain. Chem. Eng.*, 2018, **6**, 4746-4758.

[20] H. Yu, G. Guo, L. Ji, H. Li, D. Yang, J. Hu, A. Dong, "Designed synthesis of ordered mesoporous graphene spheres from colloidal nanocrystals and their application as a platform for high-performance lithium-ion battery composite electrodes", *Nano Res.*, 2016, **9**, 3757-3771.

[21] B. Wang, X. Zhang, X. Liu, G. Wang, H. Wang, J. Bai, "Rational design of Fe_3O_4@C yolk-shell nanorods constituting a stable anode for high-performance Li/Na-ion batteries", *J. Colloid Interface Sci.*, 2018, **528**, 225-236.

[22] R. Liu, T. Li, F. Han, Y. Bai, Y. Qi, N. Lun, "Thermal formation of porous Fe_3O_4/C microspheres and the lithium storage performance", *J. Alloys Compd.*, 2014, **597**, 30-35.

[23] Z. Zhou, W. Xie, S. Li, X. Jiang, D. He, S. Peng, F. Ma, "Facile synthesis of porous Fe_3O_4@C nanospheres as high-performance anode for lithium-ion battery", *J Solid State Electr.*, 2015, **19**, 1211-1215.

[24] J. Zhu, K. Y. S. Ng, D. Deng, "Porous olive-like carbon decorated Fe_3O_4 based additive-free electrodes for highly reversible lithium storage", *J. Mater. Chem. A*, 2014, **2**, 16008-160014.

[25] Y. Wang, Y. Gao, J. Shao, R. Holze, Z. Chen, Y. Yun, Q. Qu, H. Zheng, "Ultrasmall Fe_3O_4 nanodots within N-doped carbon frameworks from MOFs uniformly anchored on carbon nanowebs for boosting Li-ion storage", *J. Mater. Chem.*, 2018, **6**, 3659-3666.

[26] K. N. Kudin, B. Ozbas, H. C. Schniepp, R. K. Prudhomme, I. A. Aksay, R. Car, "Raman spectra of graphite oxide and functionalized graphene sheets", *Nano Lett.*, 2008, **8**, 36-41.

[27] L. Ma, R. Chen, G. Zhu, Y. Hu, Y. Wang, T. Chen, J. Liu, Z. Jin, "Cerium oxide nanocrystal embedded bimodal micromesoporous nitrogen-rich carbon nanospheres as effective sulfur host for lithium-sulfur batteries", *ACS Nano*, 2017, **11**, 7274-7183.

[28] Q. Xiong, Y. Lu, X. Wang, C. Gu, Y. Qiao, J. Tu, "Improved electrochemical performance of porous Fe_3O_4/carbon core/shell nanorods as an anode for lithium-ion batteries", *J. Alloys Compd.*, 2012, **536**, 219-225.

[29] T. Fujii, F. M. F. de Groot, G. A. Sawatzky, F. C. Voogt, T. Hibma, K. Okada, "In situ XPS analysis of various iron oxide films grown by NO_2-assisted molecular-beam epitaxy", *Phys. Rev. B*, 1999, **59**, 3195-3202.

[30] C. Liao, S. Wu, "Pseudocapacitance behavior on Fe_3O_4-pillared SiO_x micro-sphere wrapped by graphene as high performance anodes for lithium-ion batteries", *Chem. Eng. J.*, 2019, **355**, 805-814.

[31] B. Liu, Q. Zhang, Z. Jin, L. Zhang, L. Li, Z. Gao, C. Wang, H. Xie, Z. Su, "Uniform pomegranate-like nanoclusters organized by ultrafine transition metal oxide@nitrogen-doped carbon subunits with enhanced lithium storage properties", *Adv. Eng. Mater.*, 2017, **8**, 1702347-1702355.

[32] X. Wang, K. Chen, G. Wang, X. Liu, H. Wang, "Rational design of three-dimensional graphene encapsulated with hollow FeP@carbon nanocomposite as outstanding anode material for lithium ion and sodium ion batteries", *ACS Nano*, 2017, **11**, 11602-11616.

[33] L. Li, A. Kovalchuk, H. Fei, Z. Peng, Y. Li, N. D. Kim, C. Xiang, Y. Yang, G. Ruan, J. M. Tour, "Enhanced cycling stability of lithium-ion batteries using graphene-wrapped Fe_3O_4-graphene nanoribbons as anode materials", *Adv. Eng. Mater.*, 2015, **5**, 1500171-1500176.

[34] Y. Wang, Y. Jin, C. Zhao, E. Pan, M. Jia, "Fe_3O_4 nanoparticle/graphene aerogel composite with enhanced lithium storage performance", *Appl. Surf. Sci.*, 2018, **458**, 1035-1042.

[35] S. Zhang, L. Zhu, H. Song, X. Chen, J. Zhou, "Enhanced electrochemical performance of MnO nanowire/graphene composite during cycling as the anode material for lithium-ion batteries", *Nano Energy*, 2014, **10**, 172-180.

[36] K. Zhang, P. Han, L. Gu, L. Zhang, Z. Liu, Q. Kong, C. Zhang, S. Dong, Z. Zhang, J. Yao, H. Xu, G. Cui, L. Chen, "Synthesis of nitrogen-doped MnO/graphene nanosheets hybrid material for lithium ion batteries", *ACS Appl. Mater. Interface*, 2012, **4**, 658-664.

[37] J. Wang, J. Polleux, J. Lim, B. Dunn, "Pseudocapacitive contributions to electrochemical energy storage in TiO_2 (anatase) nanoparticles", *J. Phys. Chem. C*, 2017, **111**, 14925-14931.

[38] L. C. Liu, W. G. Pell, B. E. Conway, "Behavior of molybdenum nitrides as materials for electrochemical capacitors: comparison with ruthenium oxide", *J. Electrochem. Soc.*, 1998, **145**, 1882-1888.